UPCommons

Portal del coneixement obert de la UPC

http://upcommons.upc.edu/e-prints

Contents lists available at ScienceDirect

Flow Measurement and Instrumentation

journal homepage: www.elsevier.com

Experimental study on the impulsion port of a trochoidal wheeled pump

Gustavo Raush *, Pedro J. Gamez-Montero, Roberto Castilla, Esteve Codina

*LABSON-Department of Fluid Mechanics , Polytechnic University of Catalonia, UPC-BARCELONA**TECH,** c/Colom 11, ES-08222 Terrassa, Spain*

ARTICLE INFO

Keywords:
TRPIV
Gerotor pump
Flow pulsation
Cross-spectrum
Power spectral density
Spectrogram
Manufacturing tolerances
Trochoidal-gear
Interteeth clearances

ABSTRACT

All positive displacement pumps produce a pulsating flow. The present paper reports the experimental measurement of steady flow pulsations in the outlet of the internal wheeled pump. In the measured flow, the manufacturing tolerance are responsible of part of the spectra of the whole pulsation. Time-Resolved Particle Image Velocimetry technique has been used for this purpose. The flow pulsation measurement from a direct visualization of the velocity profile was carried out. The flow rate signal is derived from ad-hoc integration algorithm of the radial velocity profile, where the area discretization is a constant parameter that is relevant to minimize PIV errors by velocity gradients regions near the wall. Spectrographic analysis on the experimental data reveled low frequency components related with manufacturing tolerances. Measurements of this non-invasive procedure are compared with detailed CFD numerical results obtained from an improved gerotor model where manufacturing tolerances have been included. To be compared, cross-power spectral density analysis has been applied. The results reported in the paper show a method to provide a fast non-invasive flow pulsation measurement not only for pumps but also could be extended to compare aging effects of other kind of fluid power devices.

Nomenclature

Notation

A_i	generalized annulus area, m^2
CP	correlation peak
$\overline{CP}$	lowest correlation peak
$\overline{C_v}$	theoretical volumetric capacity, m^3
d_{diff}	diffraction diameter of Airy disk, m
d_i	particle image diameter, μm
d_p	particle diameter, μm
$f\#$	aperture number
λ	wave length of light source, μm
M	magnification factor
P_{xy}	cross-power spectral density
Q	volumetric flow rate, m^3/s
Q_i	instantaneous flow rate, m^3/s
Q_t	theoretical flow rate, m^3/s
q_{th}	PIV threshold factor
r_i	generalized Annulus radius, m
R	outlet radius, m
Re	Reynolds number
R_{xy}	cross-correlation sequence
S_c	surface of meshing cell, m^2
S_e	surface of an equilateral triangle, m^2
Sk	equi-volume skewness of a cell
$\overline{Sk}$	mean value of equivolume skewness of a cell
T_g	gearing period, s
TRPIV	Time-Resolved Particle Image Velocimetry
V_i	local velocity, m/s
Wr	Womersley number
μ	viscosity
ρ	density
ω	angular velocity
Z_{in}	number of inner teeth, $Z_{in}=Z-1$
Z	number of outer teeth

Subscripts

i	generic index

* Correspondence to: LABSON-Department of Fluid Mechanics, ESEIAAT, Colom 11, ES-08222 Terrassa, Spain.
Email addresses: gustavo.raush@upc.edu (G. Raush); pedro.javier.gamez@upc.edu (P.J. Gamez-Montero); robert.castilla@upc.edu (R. Castilla); esteban.codina@upc.edu (E. Codina)

http://dx.doi.org/10.1016/j.flowmeasinst.2016.10.014
Received 31 December 2015; Received in revised form 24 October 2016; Accepted 28 October 2016
Available online xxx
0955-5986/

N	latest circle index in area segmentation

1. Introduction

Hydraulic pumps are the power supplying components in hydraulic circuits. Oil pumps, including vane, internal, crescent and external gear pumps, are a critical component in many industrial applications. This type of machine is employed in a wide range of industries, from agriculture to aircraft, for supplying fuel to gas turbine engines, for instance. There are two main types: external gear pumps which use two external gears and internal gear pumps which use an external and an internal geared wheels. The present work is focused on the experimental performance of the internal gear pumps.

General principles of external and internal gear pumps are a very simple mechanism to generate flow with a minimum number of parts associated with their operation. They are based on the positive displacement machines characterized by a fixed displacement design. Characteristics like compactness, low cost and robustness, aim to geared pumps could be commonly used in cooling, lubrication and filtration systems and pumping liquids such as oil, transmission fluid and fuel. Generated rotor (gerotor) pumps are usually designed using a trochoidal geared inner rotor and an outer geared rotor. Gerotor pumps are internal rotary positive displacement devices in which the outer rotor has one tooth more than the inner rotor. The essential characteristics of gear pumps are pulsating flows that induce a pressure ripple responsible of oscillating forces within the systems and circuits [1]. The importance of flow ripple pulsation is also strongly correlated with noise level.

Numerical models of external, and internal gear pumps, have been widely studied in the literature, from the simplest 1D to more complex 3D CFD models. Gamez-Montero and Codina [2] describe a detailed dynamical model of an internal gear pump based on bond graph techniques where the numerical accuracy was experimentally validated. Vacca and Guidetti [3] provide a comprehensive description of external gear machines whatever motor or pump. Fluid dynamics, movement of gear's axes and geometric case deformation have been considered. A lumped parameter approach was chosen as the most suitable for the fluid dynamic model for the microscopic description of the flow necessary to evaluate the macro-motion of the gear's axes. Heisler et al. [4] conducted a CFD analysis of a commercial model of an external gear pump operating at high speed where the cavitation phenomenon becomes present. Castilla et al. [5] presented a detailed CFD study of the cavitation phenomena in the suction chamber of an external gear pump. The contraction of the mesh deformation and local re-meshing was carried out following an arbitrary Lagrangian-Eulerian approach. More recently, Castilla et al. [6] contribute to the understanding of the fluid-dynamics flow inside an external gear pump using a complete three-dimensional (3D) parallel simulation.

It is known that the centers of rotation suffer displacements due to fluid dynamic phenomena. Castilla et al. [7] describe the eccentricity changes undergone at the journal bearing position of an external gear pump conveniently adapted to be measured by two orthogonalized laser micrometers. The hydrodynamic theory explains that the eccentricity decreases when the pressure is sufficiently high and, the equilibrium angle presents a descendent monotone behavior when the working pressure rises [8]. The eccentricity is stronger related to the manufacturing tolerances and disturbs the dynamic behavior of the pumps. Manring and Kasaragadda [1] described the pressure and spectral characteristics of the pulse of flow related to the number of teeth of an external gear pump where the rotation axis distance is an important parameter. Mucchi et al. [9,10] go further in describing similar results, and the effects of the gear vibrations and forces applied to the casing have been analyzed.

If ideal instantaneous flow pulsation is complex, the flow pulsation in real pumps is rather difficult to simulate. Vacca and Guidetti [3] validated numerical results measuring pressure ripple at the pump outlet of external gear pumps using direct pressure measurement on a straight pipe which was blocked with a calibrated orifice discharge. So often, indirect flow ripple is used to characterize the positive displacement pumps. The most useful one is the secondary source method reported by Edge [11] which is based on the merging of the proper pump pulsation interacting with another one coming from a secondary source.

An alternative to the flow-pressure ripple measurement are the more recently developed optical-based methods. There are few references addressed to direct flow visualization in the positive displacement fluid power devices, especially in the externally geared pumps. Time-Resolved Particle Image Velocimetry, TRPIV [12–14], allows direct visualization of the flow at the outlet of the devices and provides the bandwidth necessary to pick up the pulsation with low spectral distortion. Castilla et al. [15,16] validated CFD numerical results in the aspiration chamber of a customized external gear pump with TRPIV experimental data. More recently, Stryczek et al. [17] visualize the cavitation phenomena in the trapped volume of the inlet chamber of the external gear pump for different values of the operational parameters. Moreover, Stryczek et al. pictured the influence of oil temperature on the cavitation intensity into the trapped volume of the gear pump. The method proved to be very useful for the investigation of the flow and phenomena in the gear pump as well as the model validation of the caviting phenomena and their temperature dependency. It is noteworthy that it is not a measure of the flow ripple.

Few references work in internal flows in internal geared pumps. Itoh et al. [18] describe visualizations of flow structure in a transparent body of an internal gear pump at a rotating velocity of 31 RPM. Itoh et al. carried out a procedure based on the refractive properties of the specially adapted fluid. Itoh et al. use light-reflecting tracer particles to the visualization of flow patterns in a transparent model of the pump where surfaces with special coating help to measure the fluctuation of the flow condition by brightness observation. Garcia et al. [19] used Time-Resolved Particle Image Velocimetry to obtain the interteeth instantaneous flow of the pump in a direct mode. Time-Resolved PIV confirms the numerical results of the flow pulsation of gerotor pumps.

None of the referenced works mention how the pulse of instantaneous flow can be affected due to manufacturing defects such as eccentricities and how that could be contributing to the flow ripple. Undesirable nonlinear behaviors like errors of tolerances or changes of trochoidal profiles could stimulate friction and wear debris. In order to measure instantaneous flow variations, the mass or volumetric flow procedure used must be able to measure with negligible distortion within the dynamic range of measured flow as well as the flow spectrum bandwidth.

To the knowledge of the authors a direct flow ripple visualization and spectral measurement of the outlet pulsation is still missing. In this paper, we propose an original experimental approach aimed to explore the pulsating flow at the outlet of gerotor pump with the signature of the orbital micro movements of the outer gear due to the existence of manufacturing tolerances. The Time Resolved PIV is used to obtain a direct and non-invasive measurement of the pulsating flow at the outlet of an internal wheeled hydraulic pump. This technique joints PIV and fastest image captures, recording an evenly sampled set of frames during a given period of time. If the suitably selected seeding particles have low inertia with relaxation times, the technique allows the detection of a velocity spectrum with a bandwidth of several kilohertz. TRPIV guarantees the signal of a bi-dimensional velocity map that could be used to measure the instantaneous flow indirectly. The TRPIV techniques allow an evenly sampled series of the outlet flows where the spectrum analysis can be performed. The spectrum accuracy is not only able to detect the higher harmonic components related to gear pass but

also to phenomena with origin in manufacturing tolerances. The spectrographic information and the cross-power spectral density allow to envisage manufacturing tolerances and help to predict premature wears.

Briefly, the present work is organized in the following parts. Section 2 depicts the experimental rig used in the flow visualization. The requirements of PIV seeding particles are also described together with the working fluid characteristics and its properties. Section 3 explains the numerical CFD model of the practiced gear pump and details of the mesh procedure. Section 4 sets out the experimental methodology and the integration algorithm applied on the instantaneous velocity map and used to measure the instantaneous average flow rate presents in the outlet of the gear pump. From spectrographic analysis, the low frequency component was detected. Therefore, the improvement carried on well-established CFD numerical model confirms that its origin is the presence of manufacturing tolerances. In the course, cross-power spectra density has been used to be doable the experimental and numerical comparison. Section 5 *Discussion and Results* analyzes the comparison making a proposal to future works. Finally, in Section 6 there is *Conclusions and References*.

2. Trpiv setup and experimental rig

2.1. Experimental setup

The internal flow visualization can only be carried out on transparent experimental rigs. The methacrylate body guarantees the optical transparency to carry out the visualization. The pump analyzed is a 3-D hand-made methacrylate body where the inner and outer cogwheels are both of standard manufacture. The number of teeth in the inner wheel is $Z_{in}=8$ and the outer one is $Z_{out}=9$ and the volumetric capacity of the experimental model is $C_v=9.8$ cm^3/rev. Special attention was paid to the outlet pipe, where the flow visualization was carried out. Fig. 1 shows the methacrylate body of the pump where both pipes of the inlet and the outlet ports can be clearly seen. The interrogated out port of 8 mm diameter pipe is horizontally aligned as can be observed in Fig. 1b and c.

A hydraulic circuit composes the test bench. A schema of that circuit is shown in Fig. 2. The methacrylate body of the gerotor pump is exposed to a laser head which is positioned perpendicular to the high speed camera. The test pump takes the oil from the tank situated at 1 m above. The inner cogwheel is driven by an electric motor whose rotary pulsation is controlled by a frequency electronic driver not shown. The camera and the laser are externally synchronized using a dedicated pulse generator instead of the camera has master time-base, resulting in unstable syncs [15]. As also noted by Wernet [20] it is advisable to use an external pulse generator. The camera is externally linked to a computer, where PIV image processing is carried out.

The outlet of the customized body was illuminated by the light sheet sourced by an array of solid-state laser diodes. The laser light sheet was aligned to the flow axis and the LED array was positioned 150 mm upward on the transparent body. The camera viewfinder was set up perpendicular to the observed flow direction. Multi-frame images were captured using a Photron Ultima APX-RS which has a memory capacity of 2048 images with 1024 by 1024 pixels resolution. An external function generator was set up at 3 kHz to trigger the camera and power the supply of laser head. Slightly less than 0.7 s of flow ripple history was thus produced.

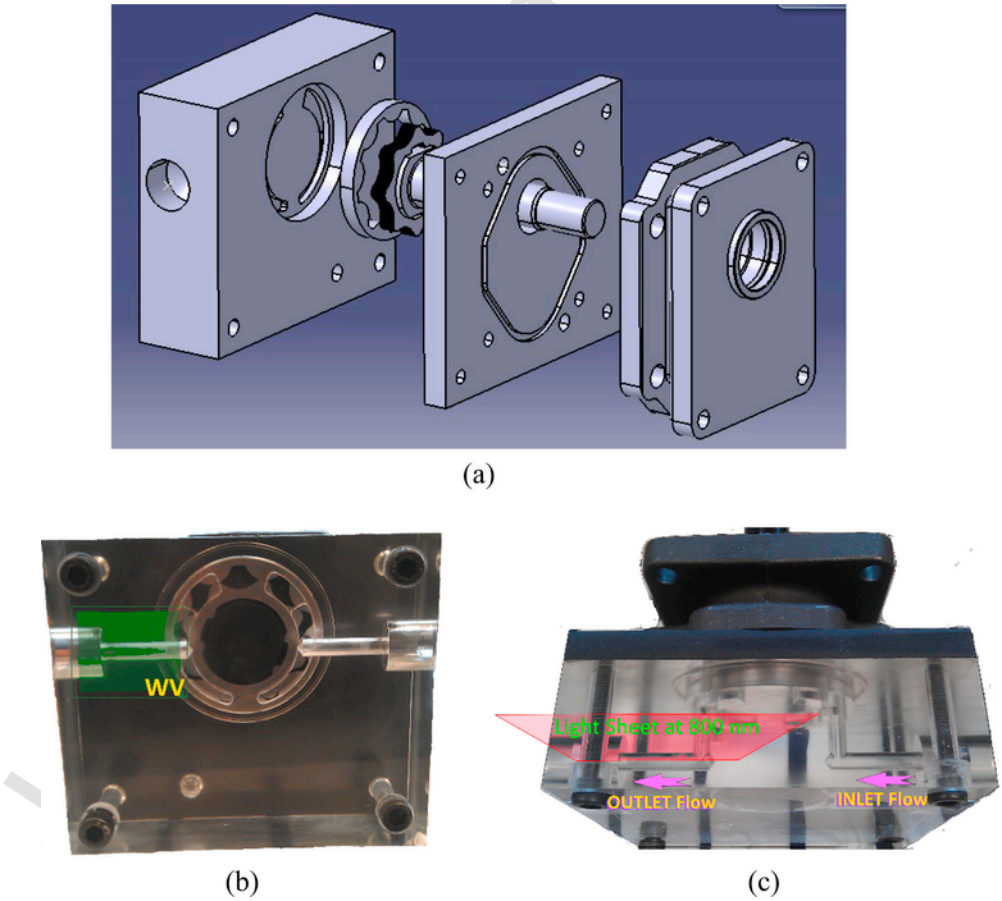

Fig. 1. Gerotor pump adapted to the experimental rig: (a) 3D design, (b) WV window visualization pointed to the outlet port and (c) vertical orientation of light sheet at 800 nm laser source.

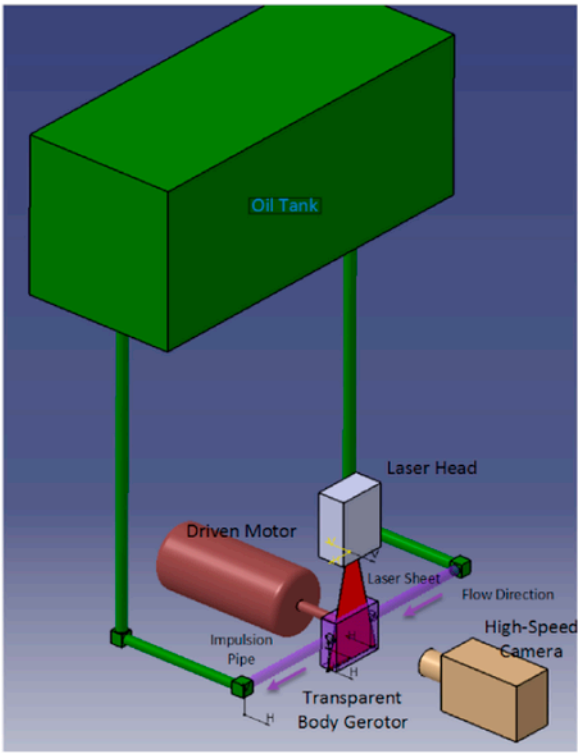

Fig. 2. Schema of the experimental rig where the camera and laser are shown.

Table 1
Characteristics of the experimental testing.

High-velocity camera		
Frame rate	3000	fps
Spatial resolution	1024×1024	pixel
Record time	0.7	s
Length Recording	2048	frames
Pixel size	17	μm
Laser		
Pulse length	50	μs
Beam dimensions	12 × 0.7	mm
Wave length	800	nm
Synchronizer		
Waveform	Square	
Mode	Continuous	
Frequency	3	kHz
Symmetry control	50	%
Output level	5	Vp-p
DC offset	0.0	V
Operating conditions of the pump		
Inner wheel rotational velocity	250	RPM
Suction/ discharge pressure	0.01/0.02	MPa
Number of outer teeth wheel, Z	9	
Number of inner teeth, Z − 1	8	
Volumetric capacity	9.8	cm^3/rev
Eccentricity	2.85	mm
Gear thickness	9.25	mm
Properties of the mineral oil		
Viscosity	$2.8 \cdot 10^{-2}$	Pa s
Density	885	kg/m^3
Tracer particles concentration	0.375	g/L

At the outlet of the pump, TRPIV enables the temporal evolution of the unsteady flow to be produced by the velocity field measurement. Particle Image Velocimetry (PIV) provides a unitary bi-dimensional velocity map from the cross-correlation of paired images. The Time Resolved PIV is an improved PIV technique where a history of bi-dimensional maps is recorded. If the sampling rate fulfills the requirements demanded by the Shannon-Hartley theorem, the aim of flow meter analysis can be performed. To make this possible, the use of high-speed cameras and faster pulsed light sheets are mandatory. By the faster harmonic spectral components of the flow ripple reported in [21], the camera and the laser diode head must be synchronized at a sampling frequency rate of at least 3 kHz. The main difficulty lays in accurately positioning the laser sheet in the meridional plane of the pipe diameter where the outlet interrogation area was established.

Table 1 summarizes the most important parameters and dimensions of the experimental rig. The transparency requirement imposes constraints on working conditions. A pressure-limiting valve was added to the discharge of the pump, which is directly connected to the oil tank placed above the outlet under study, not shown in the schema of the experimental rig. The working discharge pressure was limited to 20 kPa as well as the maximum of wheel rotation velocity was set to 250 rpm. In the developed mock, there is the risk of rotating wheels and the static methacrylate body could become jammed due to the mechanical friction reinforced by thermal expansions of the constitutive parts in contact with the working fluid. Therefore, a manufacturing tolerance bigger than industrial was carried out. The drawback of that design is higher leakage as usual which has a direct incidence on the limited outlet pressure.

2.2. Particle PIV and working fluid requirements

Particles with good dynamics are so important to capture fast velocity changes. General aspects of the particle movement and their performances can be enquired in PIV textbooks [13,22]. Nonetheless, particle dynamics are key to obtaining good accuracy of flow visualization and must be analyzed into a Lagrangian formulation [23]. Moreover, flow seeding is also critical in PIV, while homogeneous distribution is more important for producing good results and the tracers used were alginate particles described in [24]. These particles present excellent flow seeding and light scattering abilities. They guarantee good tracking of the fluid motion in both liquid and gas measurements. When they are used in liquid, there is little difference in the density of the fluid and the particles, due to their porous structure that easily absorbs the analyzing fluid. Also, alginate particles have a soft, jelly-like structure and cause no damage to the inner contact surface in the internal parts of the machines. Further details are provided by Ertürk et al. [16], where it is demonstrated that alginate particles are very suitable for PIV application in turbo-machinery, on the mineral oil is the principal working fluid. More recently, Varela et al. [25] explained in more details other PIV applications where the capability of controlling the diameter and their porosity provide great advantages in front of other seeders like air-bubbles [15].

Gaussian geometric optics limit the smallest size of the distinguishable particle. The Fraunhofer diffraction pattern [12] gauges the diameter of the Airy disk, d_{diff} represents the smallest particle image that can be obtained for a given image configuration. d_{diff} is defined,

$$d_{diff} = 2.44 f_{\#} (M + 1) \lambda \quad (1)$$

For the 200 mm telephoto lens, in the current configuration has an image magnification of M = 0.425 using an aperture of f# = 5.6, and considering the spectrum centered on λ = 0.8 μm, according to Eq. (1), the minimum diffraction distinguishable image will be d_{diff} = 15.6 μm which is comparable to the CCD Phantom pixel size of 17 μm. Image dimension of individual particles should therefore be,

$$d_p = \frac{1}{M} \sqrt{d_i^2 - d_{diff}^2} \quad (2)$$

Well established PIV practices [26] recommend a minimum number of 4–5 pixels per image particle, thus, d_i = 34 μm. Applying Eqs. (1)

and (2), the particle size should be around 70 μm in order to guarantee the Signal-to-Noise ratio in the PIV vector detection.

Scanning Electron Microscopy (SEM) shows alginate particles used in the present study where an average diameter of 50 μm has been confirmed (see [19]). The concentration in the mineral oil was set at 0.375 g/L. To ensure the appropriate concentration in the system, the mineral oil was filtered to remove particles larger than 50 μm, and the particles were added progressively in small doses to guarantee no cluster formation. In every new addition of particles to the system, the concentration is verified as suitable due to the PIV interrogation. According to Scarano [27], to ensure a good PIV analysis with a high signal-to-noise ratio in an interrogation area of 32-by-32 pixels, the density of particles should be between 5 and 15 particles, with other significant parameter being the particle relaxation time. According to [13,23] the relevant data to carry an estimated out is at Table 1 where conservatively lies $\tau \leq 30$ μs which means a bandwidth response of 30 kHz or better.

In industrialized gerotor pumps, the cogwheels are made of metal, and the working fluid is mineral oil. They are in contact with each other. In order to maintain, the real working condition, a commercial oil with a density of 885 kg/m3 and viscosity of 0.028 Pa s is used. The fluid is pumped in a closed circuit from the open elevated tank (see Fig. 2). Before to arrive at the suction chamber, the fluid enters firstly to the relaxation chamber by two opposite lateral pipes that are connected to the open elevated tank (see Fig. 2). After that, the oil is trapped between the gear teeth and body of the pump and impelled by the cogwheels. The pressurized working fluid arrives at the externally illuminated pipe which is directly connected to the outlet port. Optical properties of working fluid have been validated before in previous TRPIV experiments [16,28].

3. CFD simulation: description and details

The gear pair is contained into the housing body. Nonetheless, the sealing between different parts is not perfect. There are four different internal leakage flows: leakage flow through the trochoidal profiles due to the interteeth clearance (the gaps between gears), leakage flow through the sides of the gears and the housing and cover (an axial clearance), leakage flow through the sides of the gears and the housing direct to the oil sump (an axial clearance) and, finally, leakage flow through the gear thickness and the housing (a radial clearance). The leakages are non-constant due to manufacturing tolerance between the trochoidal profiles and the cause of the relative movement between the centers of the gears in the real pump, as due to the increased tolerances, the center of the outer wheel does not remain constant.

With the aim to study their influences in the outlet flows, several cases of pump fluid dynamics have been carried out. In the course to understand what the flow behavior into the chambers, the flow ripple at the outlet could be scrutinized. A 3D CFD model of the pump was produced where the prescribed micro-displacements between rotors and the housing of the pump have been applied to emulate the tolerance behavior.

The fluid domain is divided into three main zones: port area (inlet and outlet port included suction and discharge tubes), gearing zone located between the geared trochoidal profiles and base zone which includes the radial clearance between the outer wheel and the pump body. The CFD simulations were performed using the ANSYS FLUENT™ 12.0.16 commercial code, which is based on the finite-volume method. The 3D modeling of the pump and its meshing were produced using the GAMBIT package. The geometry of the port volume zones was meshed using a hexahedral structured mesh where the suction and discharge zone were included. For the gearing zone an unstructured deforming mesh was applied in which the edges are instantiated as springs. If the results are insufficient, the grid is locally remeshed. The deformation of the mesh is qualitatively defined with the equivolume skewness of a cell, defined as $Sk = (S_e - S_c)/S_e$, where S_c is the cell surface and S_e is the surface of an equilateral triangle with the same circumradius. In the present simulation, the maximum value of the area averaged equi-volume skewness $\overline{Sk}$ is slightly smaller than 0.28 for both inter-profile surfaces, which is less than the value of 0.5 defined as a limit for a good mesh quality deformation.

In the CFD simulation, the gear contact points of the model are indeed important. A leakage model based on a strategy developed by Gamez et al. [29] and named viscous wall cell is adopted to simulate teeth contact, i.e. the solid–solid contact point between trochoidal gears. The strategy involves two steeps. First, the Z interteeth radial clearances with the minimum size must be sought. For every time step, the wall cell that corresponds to the minimum distance between each pair of inner–outer gear teeth is searched through the mesh located at each interteeth radial clearance. Once it is located, it is labeled the contact wall cell. Secondly, the model enforces a high viscosity to each contact wall cell and, as a result, a virtual wall is created as a solid–solid boundary condition.

Even though the flow into the whole domain is very complex, mainly laminar regime is dominant. In the present simulation, the characteristic values of Reynolds numbers are from 132 to 732 in term of hydraulic diameter of the chamber at the inter-profile zone. Despite the fact that the simulation is assumed to be laminar for simplicity and computational resources saving, the numerical results have been performed by using the standard k-ε model of turbulence. The values of the transport equations practices have been guaranteed from previous works (more details have been given by Castilla et al. [6]). In the performed simulation on the proximity of gear, the mesh was refined with the aim to obtain the value of y^+ is never larger than 2. Thus, there is a laminar sublayer everywhere in the pump of the simulated velocity.

Dynamic mesh codes require a first-order scheme to be applied on the balance equations of the calculated physical magnitudes. For the continuity equation, a second-order upwind scheme was chosen because greater accuracy can be achieved when the convective term is discretized. According to software documentation, the pressure-velocity coupling scheme of Pressure-Implicit with Splitting Operators (PISO) is chosen. By means of a high-order Quadratic Upstream Interpolation for Convective Kinematic (QUICK) scheme, the spatial discretization of the momentum equations was applied. More details can be found in Gamez-Montero et al. [29].

Numerical results were accomplished with a discharge pressure similar to the experimental settings. Therefore, similar leakages are also present in the simulation. In the process of improving the numerical results, the mesh suffers deformation due to the contact point changing their position. Hence, a new meshing of the whole domain at every time step must be performed using a home-made ad-hoc code. For further details see [29].

4. Experimental procedure

4.1. TRPIV procedure

For each experimented case, there is a recording of 2048 images. This value is camera defined and only the image interval is possible to be set. Therefore, analyzing consecutive paired images there are 2048 velocity fields where the velocity profile in radius has been produced. Velocity field was computed using multi-pass cross-correlation with 50% overlap for an interrogation window of 16 pixels, providing a spatial resolution of 0.5 by 0.5 mm, almost exactly to 0.032 mm per pixel. The image recordings have been analyzed in sequentially paired images. In the process, the particle image velocimetry (PIV) image analysis is conducted using a commercial LaVision TRPIV system, DaVis™ 8.2. The multi-pass mode, starting from 64 by 64 and ending 16 by 16

interrogation area was performed. To satisfy the Nyquist sampling criterion [22], the overlapping from 75% and ending at 25% was applied. According to M = 0.425 and the window interrogation size of 16 px, the volume element of 0.32×0.32×0.7 mm^3 was interrogated approximately. Velocity vectors that have not satisfied a threshold of $q_{th} < 1.1$ were rejected, where q_{th} is a threshold factor that allows the removals of spurious vectors with origin in second correlation peaks.

The separation between velocity vectors comes from the ratio comparison between the absolute distance between the principal and secondary correlation peaks and the lowest one, $q_{th} = \left(\widehat{CP}_1 - \underline{CP}\right) / \left(\widehat{CP}_2 - \underline{CP}\right)$, where $\widehat{CP}_i$ for $i=1,2$ represents the first and second correlation peaks and $\underline{CP}$ is the lowest one, more details in [30,31].

Equalization image pre-processing of histogram normalization has been carried out. The 2048 velocity maps were then processed to obtain a velocity profile along the radius direction. Each velocity profile was integrated to carry out the instantaneous volumetric flow across the outlet area. The following Section explains the integration velocity profile.

4.2. Flow meter algorithm

The flow ripple spectrum at the outlet port can be obtained from the evolution of the velocity profile. Each sample of the mean volumetric flow was calculated from the integrated solution of the velocity profile $\mathbb{v}(r) \underset{yields}{\rightarrow} \mathbb{v}$ mapped across the plane that contains the axis of the outlet pipe. Even though this $\mathbb{v}$velocity profile is highly symmetric, the integration procedure must take into account the distortion presences. Since the measurement of the speed in areas close to the walls introduces greater uncertainty arising out of the existence of higher values of friction, the applied procedure, allows a lower propagation of error in the measurement of the total flow, especially at the pipe boundary where the velocity gradient is higher. The proposed algorithm has double advantages: the velocity gradients and the image segmentation.

It is well known that the velocity gradients are an important source of error in PIV [32]. The volumetric flow uncertainty could be minimized if the gradient error is taken into account. Therefore, firstly a non-constant segmentation of radius, starting from the region with lowest gradients, is proposed. An iso-discretization of the flow area has the property to assign bigger central region of the 2D velocity map with the lowest gradient distribution. It acts as a straigthfoward relation between the planar topology of the velocity map with the volumetric gradient distribution. Secondly, the area discretization could be adapted to the image segmentation especially needed in the interrogation process of the PIV techniques. For this purpose, the elementary area element is defined as a constant value.

The N discretization elements of section flow contribute to instant flow

$$Q = A_0 V_0 + A_1 V_1 + \cdots + A_N V_N \tag{3}$$

where A_i is the area of the i annulus, where each of them has the value of the central seeding area,

$$A_0 = A_1 = A_2 = \ldots = A_N = \pi {r_0}^2 \tag{4}$$

Replacing,

$$Q = A_0 (V_0 + V_1 + \cdots + V_N) \tag{5}$$

Each S_i has related to the areas of its concentric limiting circles. For each A_i inner and A_{i+1} outer circle area, the increment becomes,

$${r_0}^2 = \left({r_{i+1}}^2 - {r_i}^2\right) = \cdots = (R^2 - {r_N}^2) \tag{6}$$

Appling induction procedure in (6) can be proved that:

$$r_0 = \frac{R}{\sqrt{N+1}} \tag{7}$$

Each annulus of elemental area is limited by concentric circumference of radii given by:

$$r_i = \frac{\sqrt{i+1}}{\sqrt{N+1}} R \tag{8}$$

for i = 0, 1, 2, … N

The central position of each annulus is denoted by mean position of enclosing boundary circumferences, and the $\bar{r}_i$ radius is the coordinate used to map the velocity profile from the mapping $\mathbb{v}(r)$ carried out from PIV, so,

$$\bar{r}_i = \frac{\sqrt{i+1} + \sqrt{i}}{2\sqrt{N+1}} R \tag{9}$$

Fig. 3 shows the section flow discretization where each radius of the circumferential element is shown. The above described method is also known as tangential method [33].

The experimental procedure described below is focused in TRPIV applied in order to obtain the fast pulsating flow present on the outlet of a positive displacement pump, with special emphasis on the real-time study of gerotor pumps. The complete procedure is summa-

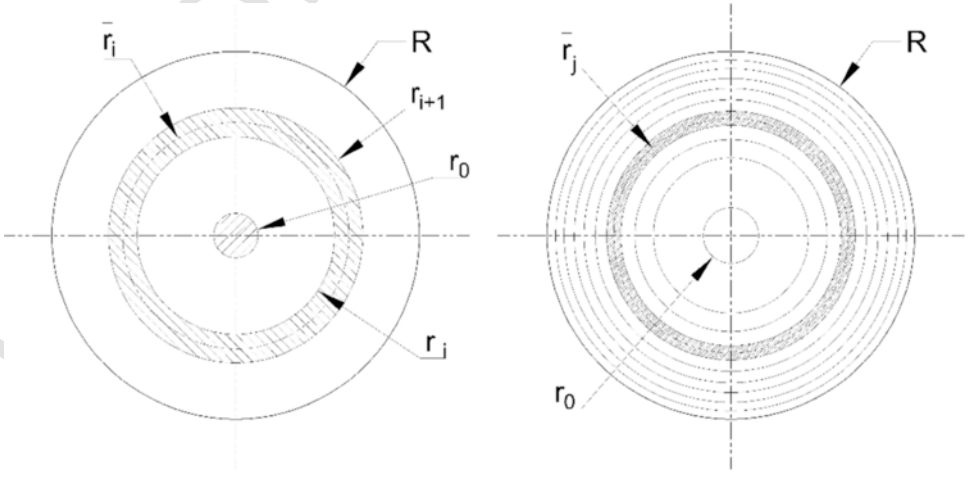

Fig. 3. Area element and its nomenclature, and evenly area sized for N = 10.

rized in the following steps: (1) For each sampling time, the velocity profile was picked up using the PIV technique, (2) the volumetric flow was measured by integration of the sample velocity profile, (3) from the flow history, the power spectral estimation was performed.

At the outlet pipe, TRPIV guarantees the evenly sampled N velocity maps. Finally, the spectrums of the experiments were compared with the corresponding spectrums of the CFD simulations for similar working conditions.

4.3. Flow measurement

Fig. 4 shows a sample of the velocity distribution along the X direction coincident with pipe axis. The sub-Fig. 4a shows the streamlines together with the map of the magnitude of velocities over. In both representations can be observed how the velocity is affected by the presence of the outlet port near the position $x = 25$ *mm*. Fig. 4b shows the spatial evolution of the velocity profile. At the entrance of the discharge pipe, near X = 22 mm, the flow suffers an abrupt change in the streamlined path, may be with some vorticity, the velocity profile is distorted. After that, the friction acts dissipating energy and from X = 15 mm, the flow shows a laminar behavior. The flow development to the laminar condition can be observed in both the right velocity profile and the velocity magnitude.

From the pre-analysis of 2048 images, the light laser sheet shows acceptable uniform distribution. Pre-image analysis was carried out where the nonlinear histogram equalization was applied. The post-processing vector map required a quality factor rejection based on dynamic range comparisons. 25 dB of dynamic range in the velocity vector was often shown in several maps measured along radial position. For a prescribed instant of the whole recording, Fig. 5 shows a highly parabolic profile in the average velocity. Error bars represent the velocity dispersion along the axial dimension of the impulsion. The statistics show similar streamline variance of velocity along the radius. Nonetheless, the biggest values are near the wall where there is highest velocity gradient that would be magnified by PIV errors. Error bars and highly parabolic shape justify the application of the assumptions made on the flow model. The average measured profile agrees completely with a Reynolds Number $Re = 75$ calculated from 0.3 m/s mean velocity of

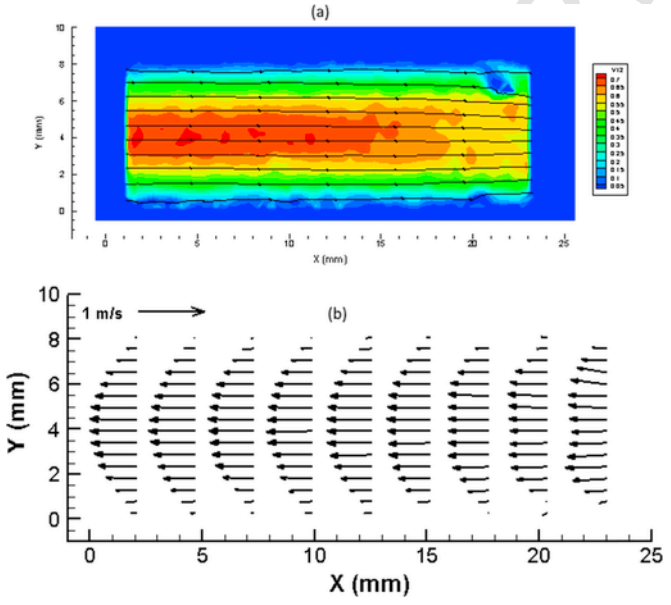

Fig. 4. Example of a sampled velocity profiles in the 8 mm outlet is shown. The subfigures depict: a) streamlines with background of the velocity magnitude, b) development of velocity profile along the flow direction.

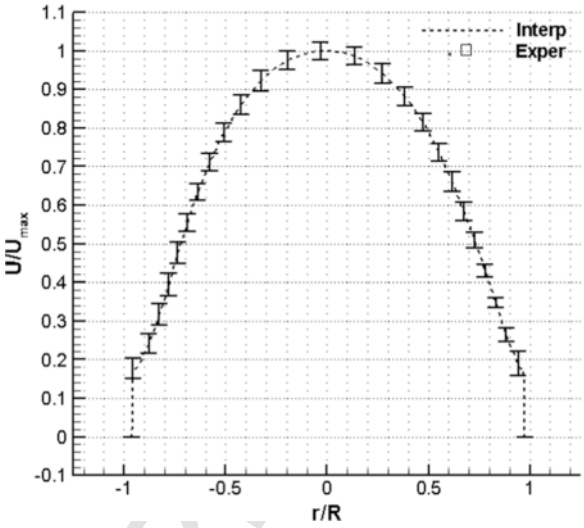

Fig. 5. Dash curve shows the interpolated profile of averaged velocity. Error bars show the statistical variance along the axial dimension of the impulsion. Biggest variances are coincident with higher gradient of velocity profile.

theoretical profile and defined by the 8 mm outlet pipe diameter. Volumetric procedures verified that a mean flow of 20 cm^3/s was produced.

Numerical and measured flow rate was compared to temporal and spectral domains. Fig. 6 shows the normalized numerical and experimental data, where numerical outputs are represented by a continuous line and the measured flow rate produced by the algorithm presented in a previous section appears on the dotted line. More details about Fig. 6 will be given in Section 5. The normalization was carried out as,

$$Q_n = \frac{Q - Q_{\min}}{Q_{\max} - Q_{\min}} \tag{10}$$

Unsteady flow modeling is an active field of study. Womersley [34] proposed an exact analytical solution to the Navier-Stokes equation for laminar and incompressible pipe flow experiencing periodic pressure gradient. The non-dimensional number, the Womersley number, $Wr = R\sqrt{\omega/\nu}$ denotes the phase lag between pressure gradient and flow. Parabolic shaped profiles are denoted by $Wr < 10$. The pulsation measured from numerical results of Fig. 6 yields $Wr = 3.6$, significantly lower than 10.

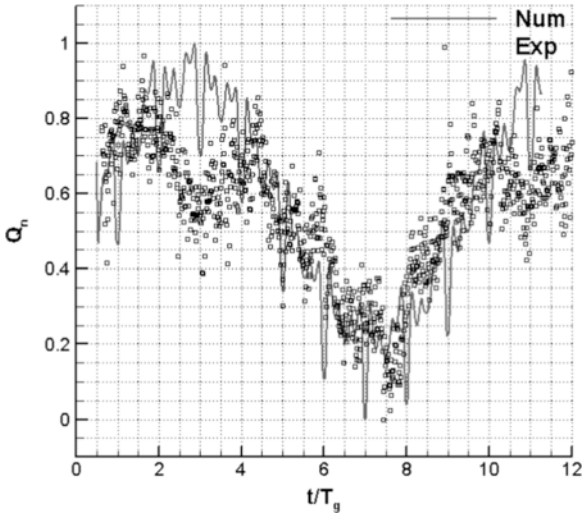

Fig. 6. Experimental and numerical normalized outlet flow. Experimental data is represented by 2048 flow values, one per average flow measurement.

4.4. Power spectral measurements

Spectra throughout the time series could be represented in 2D output where frequency and time are the main parameters. In this representation called spectrogram, each relevant frequency has a signature at the moment that appears. The amplitude is represented by the color information [35]. Often, spectrogram uses short-time Fourier transform where the signal level is represented in dB logarithmic scale defined as $dB = 10\log_{10}(S_L/S_{Ref})$. S_L is the signal itself and S_{Ref} represents a reference value. In our case, $S_L = Q_i$ and $S_{Ref} = Q_T$.

Normalized experimental flow was analyzed using spectrogram, see Fig. 7. The companion color scale shows the relevance that each frequency has. Easily appreciate frequency component of 4 Hz repeated on times of 0.25 s. Other non-less important components as 33, 55, 66, 98, 130, 134, 164 and 201 Hz are also detected. Medium and higher components are related with gear pass and flow pulsation. But the stronger 4 Hz detection might be sourced from the machining tolerance. The improved CFD model and experimental results show relevant peaks coincidences of flow pulsation. Here the cross power spectral density of two discrete-time signals based on the periodogram method, appropriately averaged using Welch's windows, was produced [37].

A second powerful tool is the cross-power spectral density. This is an effective tool for finding a predefined signal in the complex spectrums that the gerotor pump yields. The feasibility of the proposed approach was confirmed by comparing the power spectral density of both numerical and experimental signals. Several procedures for doing this can be found in the literature. Raush et al. [36] produced the spectral envelope comparison for an unevenly sampling pressure signal measured at the top of the cylinder chamber of hermetic reciprocating compressors. Mucchi et al. [21] directly compared the amplitude of power spectrums of pressure signals. In this case, experimental and numerical have been compared with simulation results carried out following the new improved numerical model of gerotor pump and described in Section 4.5 *CFD Numerical Results*.

Differences between signals can be compared even though there are different lengths, and these differences can be solved effortlessly by extracting the common part of the signal. The cross-correlation can be performed between signals with different lengths, but the identical sampling rate must be ensured [37]. The safest way to do this is by resampling the signal using the lower sampling rate.

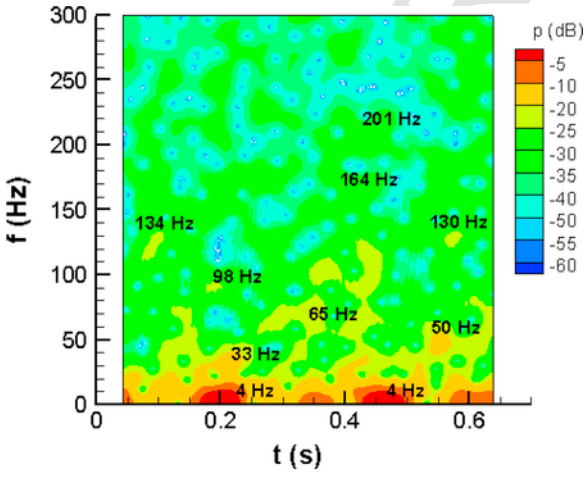

Fig. 7. Spectrogram of normalized flow.

The cross-power spectral density is

$$P_{xy}(\omega) = \sum_{m=-\infty}^{\infty} R_{xy}(m)e^{-i\omega t} \tag{11}$$

where R_{xy} is the cross-correlation sequence between both numerical and experimental signals.

But, in front of a single analysis, both spectral signals, numerical and experimental, were compared. See Fig. 8 where both flows have been correlated in their spectral amplitudes. The same frequency spectrum is observed in experimental and numerical results.

Before applying the power spectral density assessment, both signals were resampled to a common multiple frequency. In the case performed, the sampling frequency of the numerical signal was selected and any trends also removed. The experimental signal was up-sampled without contravening the Nyquist-Shannon theorem, due to the fact that an anti-aliasing low pass finite impulse response (FIR) filter was performed before applying the resampling process.

4.5. CFD numerical results

Numerical results used above have been obtained from the improved numerical model described in Section 3. In the new model, the machining tolerance has been considered. The outer gear teeth was affected by an orbital movement where the displacement parameter in X and Y directions defined on the gear plane has been carried out.

The numerical results were arranged around two relevant parameters: one, the imposed manufacturing tolerance of the eccentricity and secondly, the outlet pressure. Briefly, the pressure that equate the observed leakage is here reported. To compare the effect of the internal leakage flow, the discharge pressure imposed in the CFD simulation was raised from 0 to 54 kPa on the change at outlet pressure. Results show that the internal leakages affect the outlet flow by more than 30%.

The results are presented in the Fig. 9 and Fig. 10 using the normalized time t/T_g and the normalized flow Q_i/Q_t. Instantaneous flow Q_i has been rationalized with the theoretical flow $Q_t = \omega C_v$ where ω is the rotational velocity of the shaft during the test. C_v is the theoretical volumetric capacity. Time was normalized with the gearing period defined as $T_g = 1/[\omega(Z-1)]$ where Z is the number of external gear teeth. Fig. 9 shows the numerical results of the pressurized outlet with fixed eccentricity of 2.85 mm, SIM1. SIM2 reproduces the condition of or-

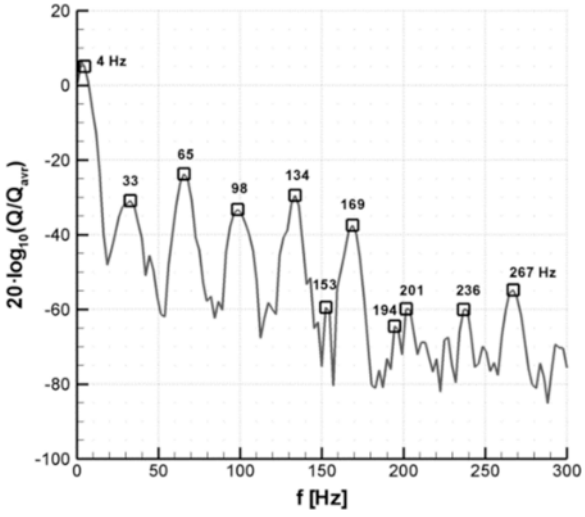

Fig. 8. Cross correlated power spectral density between numerical and experimental flow rate.

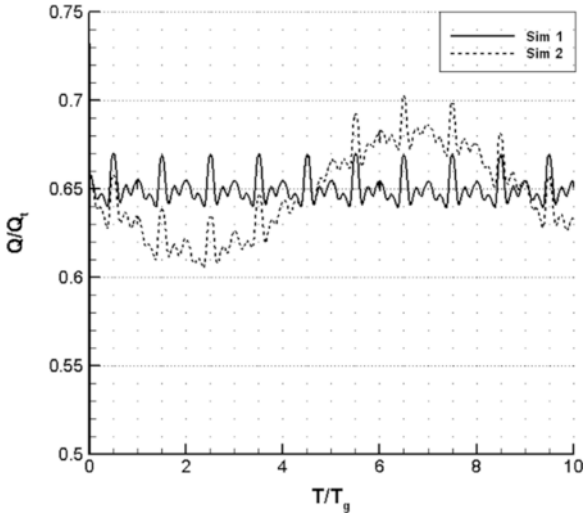

Fig. 9. Normalized flow at the pressurized outlet with fixed eccentricity (SIM1) and with moved eccentricity (SIM2).

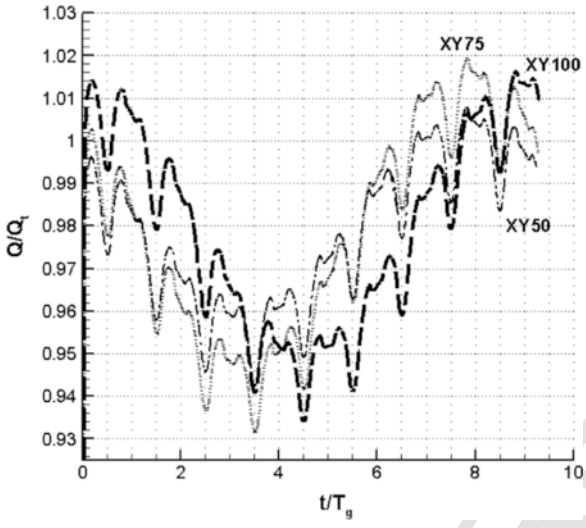

Fig. 10. CFD (non fixed centers) flow in the outlet discharge. The eccentricity is reflected for three prescribed movements.

bital motion which is experience by the outer wheel due to machining tolerance. Notably, the presence of movement in the eccentricity shows significant difference in normalized flow, see Fig. 9. Fig. 10 shows the change in the outlet discharge due to different tolerances. The analyzed displacements coplanar to wheels have been in X, Y and summation of both, XY. For brevity, herein only the summation XY is analyzed.

Clearly, SIM2 shows the influence of the eccentricity displacements 4 Hz low component which is directly related to the manufacturing tolerances. There are remarkably differences in the flow evolution between numerical cases where the manufacturing tolerances are considered or not. Moreover, Fig. 10 shows the influence of uncertainty in the manufacturing tolerance between wheels. Three different values of 50, 75 and 100 μm have been simulated with a time interval of 30 μs, labeled: XY50, XY75 and XY100 respectively. The gear teeth pulsations on the chopped flow can be clearly appreciated. The fundamental frequency component of 33 Hz related to gear pass can be observed in both. But, numerical results show the importance of biggest tolerance 100 μm in the flow variation in front of the other two, see Fig. 10. There is also more phase shifting between flow rate ripple. The 4 Hz component continues dominating.

In the previous Section 4.4 spectral methods of the cross-power spectral density show in Fig. 8 how both signals have similarity where the 4 Hz component directly related with manufacturing tolerance is strongest one.

5. Discussion and results

Flow measurements by direct and non-invasive methods are invariably a great challenge. Furthermore, if the flow presents peaks around the mean value, the challenge is even more difficult. Therefore, it is often easier to obtain information from the frequency domain than the time domain. Two signals can also be compared by cross-correlation of their spectrums. The spectrum signatures thus provide not only information from the signal itself but also about the system itself.

Valuable information about the inner working conditions can be obtained from ripple flow outputs. TRPIV provides the direct noninvasive flow velocity, thus enabling the outlet flow rate to be integrated. Fast image capture provides the sampling rate to pick up the instantaneous variation of flows, and the spectral information is therefore retained.

Notably, the peaks of cross spectra show the components related to the internal wheel, represented by its teeth number (see Table 1). The internal wheel at 250 RPM with $Z_{in}=8$ teeth gives pulsation of 33.3 Hz as the fundamental frequency. After spectrum processing, the values show not only the fundamental component to the 7th harmonics of the teeth pulsation summarized in 33, 66, 98, 134, 169, 201, 236 and 267 Hz of signal peaks but also 4 Hz peak. Similar values are observed in the spectrogram of Fig. 7 which was only obtained with experimental data. In both cases, component confirms the presence of manufacturing tolerances and their influence on the final flow (see Fig. 7 and Fig. 8).

It is interesting to appreciate that there is a notable presence of secondary peaks at 153 and 194 Hz that would be related to the harmonic modulation of the pulsation flow and the planetary oscillation of the internal and external wheels. Their presence is also confirmed in the spectrogram of Fig. 7. The aliasing phenomenon was considered in the proposed approach. This phenomenon is especially relevant not only to the image sampling rate but also to the low-pass frequency response of the particles. The bandwidth under study is considerably lower than the image camera sampling and higher than the particle bandwidth of greater than 30 kHz.

The final and more direct time comparative is depicted in Fig. 6. Despite the fact that there is a high match between numerical and experimental results, there are significant discrepancies in the areas of high flows. As shown in Fig. 6, the data present a significant fall in the value of the experimental flows that could be related with the presence of important leakages. In the methacrylate body, the practiced manufacturing tolerances have been especially high compared with standard unit. The risk of unwanted frictions plays in the design of the mock-up.

In future works, the authors will explore the differences between spectrograms information and different manufacturing tolerances. The spectrogram data could be used like a fingerprint of each case but not only for tolerances also aging by use. The proposed method would allow a real-time measurement of the instantaneous flow at the outlet. Searching similarities between the actual measurements and previously stored patterns, the aging could be detected. The TRPIV signal is an appropriated tool for this objective.

6. Conclusions

This paper presents the results of a new experimental approach aimed to obtain direct and non-invasive measurement of the pulsating flow of internal wheeled hydraulic pumps. To measure the flow rate at the outlet of a gerotor pump, Time-Resolved Particle Image Velocimetry (TRPIV) was carried out. In order to analyze the influences of the

mechanization tolerances on the outlet ripple, TRPIV follows the appropriate image sampling that Nyquist-Shannon theorem demands. The instantaneous bi-dimensional velocity map on the axial aligned diametric plane was integrated following an ad-hoc algorithm of an iso-discretized sampled crossing area that minimizes the error by gradient near the pipe wall. The experimental signal was individually analyzed by spectrogram but was also cross-power spectrum compared with CFD numerical results of the methacrylate mock-up of the full-scaled pump that was integrated in the experimental rig. The experimental approach explained here could be extended to obtaining direct and instantaneous noninvasive measurements of the flow pulsations at the outlet of any hydraulic devices. The complex spectrum of the flow could be stored for future searches on extended databases of actual and future designs. Moreover, the pattern matching between numerical and experimental results could be extended to seeking potentially faulty or aging behaviors.

Acknowledgements

This project DPI2013-42031-P research program receives financial support from the Ministry of Economy and Competitiveness of Spain and is co-financed by FEDER EU financial support. The authors wish to acknowledge these financial supports. The authors would also like to acknowledge the support of AMES (Spain) and Pedro Roquet (Spain). Finally, special thanks to the von Karman Institute for Fluid Dynamics (Belgium) for authorizing the use of DaVis™ tools.

References

[1] N.D. Manring, S.B. Kasaragadda, The theoretical flow ripple of an external gear pump, J. Dyn. Syst. Meas. Control Trans. ASME 125 (2003) 396–404, http://dx.doi.org/10.1115/1.1592193.

[2] P. Gamez-Montero, E. Codina, Flow characteristics of a trochoidal-gear pump using bond graphs and experimental measurement. Part 1, Proc. Inst. Mech. Eng. Part I J. Syst. Control Eng. 221 (2007) 331–346, http://dx.doi.org/10.1243/09596518JSCE250.

[3] A. Vacca, M. Guidetti, Modelling and experimental validation of external spur gear machines for fluid power applications, Simul. Model. Pract. Theory 19 (2011) 2007–2031, http://dx.doi.org/10.1016/j.simpat.2011.05.009.

[4] A.S.Heisler, J.J.Moskwa, F.J.Fronczak, Simulated helical gear pump analysis using a new CFD Approach, in: Proceedings of Symp. Parts A, B C, ASME, Vail, Colorado USA, vol. 1, 2009, pp. 445–455. ⟨http://dx.doi.org/10.1115/FEDSM2009-78472⟩.

[5] R. Castilla, P.J. Gamez-Montero, N. Erturk, A. Vernet, M. Coussirat, E. Codina, Numerical simulation of turbulent flow in the suction chamber of a gearpump using deforming mesh and mesh replacement, Int. J. Mech. Sci. 52 (2010) 1334–1342, http://dx.doi.org/10.1016/j.ijmecsci.2010.06.009.

[6] R. Castilla, P.J. Gamez-Montero, D. del Campo, G. Raush, M. Garcia-Vilchez, E. Codina, Three-dimensional numerical simulation of an external gear pump with decompression slot and meshing contact point, J. Fluids Eng. 137 (2015) 41105, http://dx.doi.org/10.1115/1.4029223.

[7] R. Castilla, M. Gutes, P.J. Gamez-Montero, E. Codina, Experimental study of the shaft motion in the journal bearing of a gear pump, J. Eng. Gas. Turbines Power 131 (2009) 52502, http://dx.doi.org/10.1115/1.3078202.

[8] R. Castilla, M. Gutes, P.J. Gamez-Montero, E. Codina, Numerical analysis of the shaft motion in the journal bearing of a gear pump, J. Eng. Gas. Turbines Power 132 (2010) 12504, http://dx.doi.org/10.1115/1.3126771.

[9] E. Mucchi, G. Dalpiaz, A. Rivola, Dynamic behavior of gear pumps: effect of variations in operational and design parameters, Meccanica 46 (2011) 1191–1212, http://dx.doi.org/10.1007/s11012-010-9376-y.

[10] E. Mucchi, A. Rivola, G. Dalpiaz, Modelling dynamic behaviour and noise generation in gear pumps: procedure and validation, Appl. Acoust. 77 (2014) 99–111, http://dx.doi.org/10.1016/j.apacoust.2013.10.007.

[11] K.A.Edge, D.N.Johnston, The secondary source method for the measurement of pump pressure ripple characteristics. Part 1: description of method, in: Proceedings Instn. Mech. Engrs., vol. 204, 1990, pp. 33–40, 1990.

[12] M. Raffel, C.E. Willert, S.T. Wereley, J. Kompenhans, Particle Image Velocimetry: A Practical Guide, Springer, Berlin, 2007.

[13] R.J. Adrian, J. Westerweel, Particle Image Velocimetry, Cambridge University Press, Berlin, Heidelberg, 2008http://dx.doi.org/10.1007/978-3-540-73528-1.

[14] A. Vogel, W. Lauterborn, Time resolved particle image velocimetry, Opt. Lasers Eng. 9 (1988) 277–294, http://dx.doi.org/10.1016/S0143-8166(98)90008-2.

[15] R. Castilla, J. Wojciechowski, P.J.J. Gamez-Montero, A. Vernet, E. Codina, Analysis of the turbulence in the suction chamber of an external gear pump using time resolved particle image velocimetry, Flow Meas. Instrum. 19 (2008) 377–384, http://dx.doi.org/10.1016/j.flowmeasinst.2008.06.005.

[16] N. Ertürk, A. Vernet, J. Pallares, R. Castilla, G. Raush, Small-scale characteristics and turbulent statistics of the flow in an external gear pump by time-resolved PIV, Flow Meas. Instrum. 29 (2013) 52–60, http://dx.doi.org/10.1016/j.flowmeasinst.2012.09.004.

[17] J. Stryczek, P. Antoniak, O. Jakhno, D. Kostyuk, A. Kryuchkov, G. Belov, L. Rodionov, Visualisation research of the flow processes in the outlet chamber–outlet bridge–inlet chamber zone of the gear pumps, Arch. Civ. Mech. Eng. 15 (2015) 95–108, http://dx.doi.org/10.1016/j.acme.2014.02.010.

[18] T. Itoh, Y. Murai, Y. Ueno, H. Oiwa, N. Miyagi, F. Yamamoto, Visualization of internal flow in an inscribed trochoid gear pump, Trans. Vis. Soc. Jpn. 26 (2006) 27–32, http://dx.doi.org/10.3154/tvsj.26.27.

[19] M. Garcia-Vilchez, P. Gamez-Montero, E. Codina, R. Castilla, G. Raush, J. Freire, C. Rio, Computational fluid dynamics and particle image velocimetry assisted design tools for a new generation of trochoidal gear pumps, Adv. Mech. Eng. 7 (2015) http://dx.doi.org/10.1177/1687814015592561.

[20] M.P. Wernet, Temporally resolved PIV for space–time correlations in both cold and hot jet flows, Meas. Sci. Technol. 18 (2007) http://dx.doi.org/10.1088/0957-0233/18/7/C01.

[21] E. Mucchi, G. Cremonini, S. Delvecchio, G. Dalpiaz, On the pressure ripple measurement in variable displacement vane pumps, J. Fluids Eng. 135 (2013) 91103, http://dx.doi.org/10.1115/1.4024110.

[22] J. Westerweel, G.E. Elsinga, R.J. Adrian, Particle image velocimetry for complex and turbulent flows, Annu. Rev. Fluid Mech. 45 (2013) 409–436, http://dx.doi.org/10.1146/annurev-fluid-120710-101204.

[23] A. Melling, Tracer particles and seeding for particle image velocimetry, Meas. Sci. Technol. 8 (1997) 1406–1416, http://dx.doi.org/10.1088/0957-0233/8/12/005.

[24] N.Ertürk, A.Düzgun, J.Ferrè, S.Vareal, A.Vernet, Alginate flow seeding microparticles for use in Particle Image Velocimetry (PIV), in: Proceedings of the 10th International Symp. Part. Image Velocim. – PIV13. (July 1–3), Delft, The Netherlands, 2013.

[25] S. Varela, I. Balagué, I. Sancho, N. Ertürk, M. Ferrando, A. Vernet, Functionalised alginate flow seeding microparticles for use in Particle Image Velocimetry (PIV), J. Microencapsul. 33 (2016) 153–161, http://dx.doi.org/10.3109/02652048.2016.1142016.

[26] F. Scarano, M.L. Riethmuller, Iterative multigrid approach in PIV image processing with discrete window offset, Exp. Fluids 26 (1999) 513–523, http://dx.doi.org/10.1007/s003480050318.

[27] F. Scarano, Iterative image deformation methods in PIV, Meas. Sci. Technol. 13 (2002) R1–R19, http://dx.doi.org/10.1088/0957-0233/13/1/201.

[28] N. Ertürk, A. Vernet, R. Castilla, P.J. Gamez-Montero, J.A. Ferre, Experimental analysis of the flow dynamics in the suction chamber of an external gear pump, Int. J. Mech. Sci. 53 (2011) 135–144, http://dx.doi.org/10.1016/j.ijmecsci.2010.12.003.

[29] P.-J. Gamez-Montero, R. Castilla, D. del Campo, N. Erturk, G. Raush, E. Codina, Influence of the interteeth clearances on the flow ripple in a gerotor pump for engine lubrication, Proc. Inst. Mech. Eng. Part D J. Automob. Eng. 226 (2012) 930–942, http://dx.doi.org/10.1177/0954407011431545.

[30] J. Westerweel, Efficient detection of spurious vectors in particle image velocimetry data, Exp. Fluids 16–16 (1994) 236–247, http://dx.doi.org/10.1007/BF00206543.

[31] J. Westerweel, F. Scarano, Universal outlier detection for PIV data, Exp. Fluids 39 (2005) 1096–1100, http://dx.doi.org/10.1007/s00348-005-0016-6.

[32] P. Meunier, T. Leweke, Analysis and treatment of errors due to high velocity gradients in particle image velocimetry, Exp. Fluids 35 (2003) 408–421, http://dx.doi.org/10.1007/s00348-003-0673-2.

[33] L.A. Salami, Errors in the velocity-area method of measuring asymmetric flows in circular pipes, in: Mod. Dev. Flow Meas., 1971, pp. 381–400.

[34] J.R. Womersley, Method for the calculation of velocity, rate of flow and viscous drag in arteries when the pressure gradient is known, J. Physiol. 127 (1955) 553–563, http://dx.doi.org/10.1113/jphysiol.1955.sp005276.

[35] A.V. Oppenheim, R.W. Schafer, J.R. Buck, Discrete-time Signal Processing, 1999.

[36] G. Raush, J. Rigola, D. Pérez-Segarra, A. Oliva, A novel sigma–delta ADC application oriented to test hermetic reciprocating compressors, Meas. Sci. Technol. 15 (2004) 2207–2214, http://dx.doi.org/10.1088/0957-0233/15/11/005.

[37] M.B. Priestley, Spectral Analysis and Time Series, 11th ed., Elsevier Ltd., Manchester, 1981.